Particlelike valleytronics in graphene

Thomas Fabian, Lukas Walzek, Joachim Burgdörfer, and Florian Libisch [*]

Institute for Theoretical Physics, Vienna University of Technology, A-1040 Vienna, Austria, E.U.

George Datseris

Max Planck Institute for Meteorology, Department of Atmosphere in the Earth System, Hamburg, Germany, E.U.

Particlelike scattering states allow for noiseless transport through quantum dots by closely retracing bundles of classical trajectories. We identify such raylike states for electron transport through graphene ribbons. Remarkably, we find that these quasiclassical scattering states can be unambiguously associated with well-defined quantum numbers of the valley degree of freedom specific to graphene. Trigonal warping—i.e., deviations of the band structure from a perfectly isotropic two-dimensional Dirac equation due to the hexagonal lattice structure—results in preferred propagation directions and scattering time delays that depend on the valley the particlelike wave travels in. By implementing a truncated mode basis of Bloch states, we achieve simulations of micrometer-sized quantum dots starting from an atomic-scale tight-binding Hamiltonian.

I. INTRODUCTION

Coherent and ballistic electron transport through mesoscopic and nanoscopic structures is fully characterized by the scattering (S) matrix of quantum dynamics. Within the Landauer-Büttiker description of quantum transport [1,2], conductance and conductance fluctuations can be extracted from elements of the S or T (transmission) matrix. Two-dimensional (2D) open quantum dots with hard-wall confinement, often referred to as quantum billiards, have served in the past as a paradigm for studying the crossover from quantum to classical ballistic transport [3–6]. When the system size is less than the elastic mean free path λ_e, the shape of the wall directly determines the motion of electrons and the geometry of the boundary is strongly reflected in transport properties. For ultraclean graphene sheets sandwiched between boron nitride, λ_e may well exceed several microns [7]. We study in the following transmission through micron-sized quantum dots realizable in experiments.

Particlelike scattering states have been identified in transport through billiards that mostly feature regular dynamics [8]. They are capable of accurately retracing bundles of topologically equivalent classical trajectories [9] whose volume in phase space is sufficiently large as to accommodate one or more quantum states. Particlelike or, more precisely, raylike states can be viewed as complementary to "scarred" states identified in chaotic cavities [10,11]. While both classes of states feature clear imprints of classical trajectories on wave functions, the underlying mechanism for their formation and resulting properties are fundamentally different. Scars, meanwhile also investigated in graphene billiards [12,13], are associated with isolated, unstable periodic orbits in bound

chaotic systems. In open cavities, coupling of these trajectories featuring infinite dwell times to the leads is mediated only by dynamical tunneling or diffractive scattering. Scarred states, therefore, give rise to narrow long-lived resonances and in general do not contribute significantly to transport through open cavities. By contrast, the classical ray states we explore in the following directly connect the open leads and therefore prominently contribute to transport [Fig. 1(e)]. The trajectories associated with the ray states are not isolated but form bundles in regular systems covering a sizable volume in phase space in units of h^M (h: Planck quantum, M: number of degrees of freedom) sufficient to accommodate noise-free scattering states. Unlike for scars, the hallmark of trajectories associated with ray states are their short dwell times inside the cavity contributing to the smooth nonresonant continuum.

Particlelike or raylike scattering states have been identified for free-particle motion with quadratic dispersion $E \propto k^2$, and for deBroglie wavelengths λ_D small compared to the linear dimension of the lead width W, $\lambda_D \ll W$ (see Fig. 1). In this regime a large number N of scattering channels is open, $N = 2W/\lambda_D \gg 1$, allowing for a suitable coherent superposition of incoming scattering channel functions that form quasiclassical scattering states. Such raylike scattering states hold the promise of novel applications including noiseless transport and low-energy geometric electron optics in condensed matter. In the present work we generalize the concept of particlelike scattering states to transport through graphene quantum dots and to micrometer-scale graphene ribbons. In this context, graphene is of particular interest for several reasons [14]: the free-particle motion inside the quantum dot is replaced by Bloch wave packets on a hexagonal lattice, the quadratic dispersion is replaced by a linear dispersion $E \propto k$ in the vicinity of the Dirac point making thereby closer contact to ray optics, and the electronic band structure of graphene

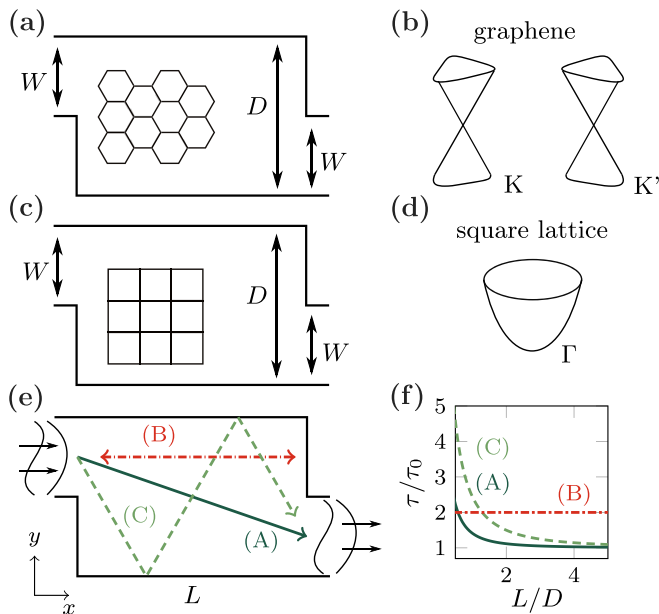[*]florian.libisch@tuwien.ac.at

125419-1

FIG. 1. Two-dimensional rectangular scattering structures with length L and width D attached to entrance and exit leads with width W defining the asymptotic scattering channels. Graphene ribbon (a) with bulk Dirac cone band structure (b), and square lattice (c) with bulk parabolic band structure (d). Typical classical paths representing bundles traversing the structure are shown in (e): the direct transmission path (A), the direct reflection path (B), and a transmission path (C) which scatters multiple times at the boundaries before reaching the exit. (f) The corresponding classical dwell times τ_{cl} for the path bundles depicted in (e) in units of the lower bound for the transit time $\tau_0 = L/v$ as a function of L/D.

features an additional valley degree of freedom associated with the two nonequivalent corners K and K' of the Brillouin zone. We explore the influence of this discrete quantum number on the quasiclassical ray states.

Key property of particlelike scattering states is that they are eigenstates of the Eisenbud-Wigner-Smith (EWS) time-delay operator [15–17]

$$Q(E) = -i\hbar S^{\dagger}(E)\frac{\partial}{\partial E}S(E), \qquad (1)$$

with eigenvalues τ^{EWS} closely approximating the transit time of classical particles traveling through the quantum dot along the corresponding ray. Moreover, they are eigenstates of the transmission operator $\hat{T}$ with eigenvalues near the endpoints of the spectrum, i.e., either $t_j = 1$ (perfect transmission) or $t_j = 0$ (no transmission at all but perfect reflection).

In this work we calculate the spectrum of the time-delay operator for large rectangular graphene quantum dots with a width D of up to 1 μm. Calculating the scattering matrix for such large-scale structures starting from an atomic tight-binding Hamiltonian requires the implementation of a new truncated mode basis expansion. We find that quasiclassical trajectory bundles can be doubly occupied by ray-scattering states with different valley quantum numbers. Despite the size of the structure, the atomistic scale—via the orientation of the graphene lattice—does play an important role in determining the resulting scattering dynamics. Trigonal warping—the

deviation of the band structure of graphene from a perfectly isotropic Dirac cone at larger energies [14]—leads to pronounced differences in dwell times in the two valleys and to a preference for certain propagation directions. In order to relate the real-space trajectory bundles to features of the band structure we employ a Husimi representation [18] for ray-scattering states. It reveals the role of the valley degree of freedom and the origin of the strong directional dependence. For numerical efficiency we focus here on rectangular ribbons well described by our truncated mode basis expansion.

This paper is organized as follows: in Sec. II we briefly review the atomic-scale tight-binding description of graphene employed in the present simulation and the methods for constructing and analyzing ray-scattering states. The new truncated mode basis expansion which enables simulations of micrometer-sized graphene ribbons and dots is introduced in Sec. III. Results for the spectrum of a time-delay operator and of ray states are given in Sec. IV where we also compare the spectrum for the hexagonal lattice of graphene with those for a square lattice with quadratic dispersion near the Γ point. We conclude with a short summary and outlook in Sec. V.

II. TIGHT-BINDING APPROACH AND TIME-DELAY SPECTRA

We model the two-dimensional scattering structures (Fig. 1) by a tight-binding Hamiltonian of the form

$$\mathcal{H} = \sum_i^{n_o} \varepsilon_i \hat{c}_i^{\dagger} \hat{c}_i + \sum_{\langle i,j \rangle} \gamma_{ij} \hat{c}_i^{\dagger} \hat{c}_j, \qquad (2)$$

with $\hat{c}_i^{\dagger}$ ($\hat{c}_i$) the creation (annihilation) operators of a quasiparticle at the atomic site i with position r_i, $\epsilon_i = \langle i | \mathcal{H} | i \rangle$ the on-site (diagonal) matrix elements. For graphene [Fig. 1(a)] we include third-nearest neighbor tight-binding coupling [19], with $\epsilon_i = -0.126$ eV and hopping matrix elements $\gamma_{ij} = \langle i | \mathcal{H} | j \rangle$ parametrized by the distance $|r_i - r_j|$ between sites. The third-nearest neighbor approach is parametrized by three couplings γ_i between ith nearest neighbors ($i = 1, \ldots, 3$), $\gamma_1 = -3.145$ eV, $\gamma_2 = -0.042$ eV, $\gamma_3 = -0.35$ eV. These parameters are derived from *ab initio* DFT simulations of the graphene band structure [20]. They accurately reproduce the band structure near the Dirac point as well as the trigonal warping correction at higher energies [schematically shown in Fig. 1(b)]. The finite value of the on-site matrix element ensures that the Dirac point remains at $E = 0$ after including all interactions. Only in first-nearest-neighbor tight-binding approximation does the on-site matrix element vanish due to the perfect electron-hole symmetry of the band structure in this limit. For a comparison with transport through a structure featuring quadratic dispersion we also simulate a ribbon built up from a square lattice [Figs. 1(c) and 1(d)]. Here we use a simple nearest-neighbor tight-binding parametrization with nearest-neighbor hopping $\gamma_1 = \hbar^2/(2m^*a^2)$ with a the lattice spacing and m^* the effective mass.

We consider rectangular geometries of length L and width D attached to leads of width W on the top left and lower right part of the ribbon [Figs. 1(a), 1(c) and 1(e)]. For graphene, zigzag edges are along the ribbon (x axis), armchair edges

perpendicular to it (y axis). The formation of quasiclassical particlelike or ray scattering states requires relatively large quantum numbers, i.e., a large number of open modes in the leads,

$$N \approx 4W/\lambda_D = 2Wk/\pi \gg 1, \tag{3}$$

corresponding to relatively high energies, as E scales for graphene as $E = v_F \hbar k \approx \pi \hbar v_F N/(2W)$. Consequently, quasiclassical ray states can be increasingly accurately formed for $N \gg 1$. Therefore, simulating particlelike states requires, on the atomic scale, wide leads such that the electron wavelength is much larger that the atomic spacing ($\lambda \gg a$), yet much smaller than the linear dimension of the structure ($\lambda \ll W, D$). We consider graphene ribbons with widths $D = 60$ nm, 250 nm, and 1 μm and lengths ranging from $L = 0$ to $L = 5.5 D$. In the simulations presented below we choose $D = 2W$ (see Fig. 1). We typically consider energies where 99 transverse channels are open in the leads. For the system with parabolic dispersion used for comparison we choose the effective mass accordingly. For the narrowest ribbon with $D = 60$ nm and a lead width $W = 30$ nm at an energy of $E = 1.5$ eV above the Dirac point the number of open modes is reduced to $N = 69$.

Typical classical trajectories representing bundles contributing to transmission (A,C) and reflection (B) are shown in Fig. 1(e). Each bundle comprises the ensemble of trajectories that can be generated by a continuous variation of the y coordinate of the starting point at the entrance lead and by the variation of the injection angle θ subject to the constraint that the topology of the representative trajectory such as direct transmission (A) or single-bounce reflection (B) remains invariant.

Our goal is now to search for those quantum scattering states whose EWS time delays closely corresponds to the classical dwell times of corresponding bundles inside the structure. To this end, we calculate the spectrum of the EWS time-delay matrix given in terms of the S matrix [Eq. (1)], where S is a $2N \times 2N$ matrix consisting of four $N \times N$ blocks:

$$S(E) = \begin{pmatrix} r(E) & t'(E) \\ t(E) & r'(E) \end{pmatrix}, \tag{4}$$

denoting the reflection (r) and transmission (t) matrices for flux incoming from the left (unprimed) or right (primed) lead (see Fig. 1). The corresponding block structure of the time-delay matrix Q is written as

$$Q(E) = \begin{pmatrix} Q_{ll}(E) & Q_{rl}(E) \\ Q_{lr}(E) & Q_{rr}(E) \end{pmatrix}. \tag{5}$$

In Eq. (5) $Q_{ll}(E)$ and $Q_{rr}(E)$ denote the time-delay matrix for scattering states purely incoming either from the left (ll) or right (rr) while the off-diagonal blocks Q_{lr} and Q_{rl} account for superpositions between left and right incoming scattering states.

Quasiclassical ray states are now eigenstates of Q,

$$Q(E)|\tau_i^{EWS}\rangle = \tau_i^{EWS}|\tau_i^{EWS}\rangle, \tag{6}$$

with the additional constraint that the contribution from nonclassical superpositions between states incoming from the left and right vanish. Focusing on the following (without loss of
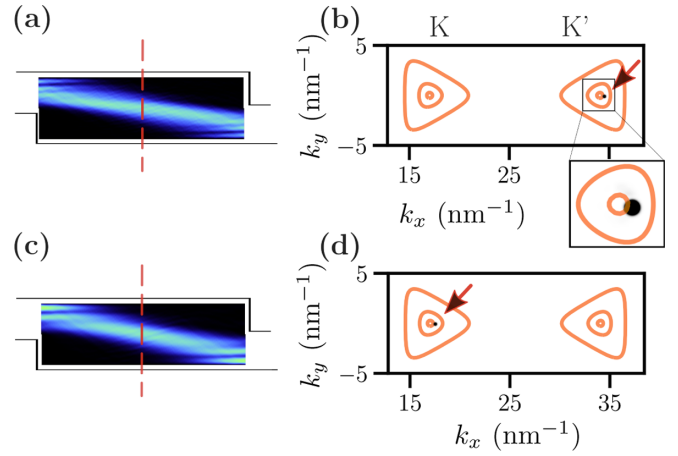

FIG. 2. Left panels (a) and (c): real space wave function probabilities of selected Eisenbud-Wigner-Smith time-delay operator eigenstates for the 1 μm wide and 5 μm long graphene ribbon. The Husimi distributions (right panels) are evaluated at $x = L/2$, averaged over y, as indicated in (a) and (c) by the red dashed line. (b) and (d) Husimi distribution of the corresponding wave functions on the left in black, with contour lines (orange) of bulk band structure at $E = 0.15$, 0.59, 1.49 eV. The black spots (see arrows and magnification) represent more than 90% of the total weight of the strongly localized Husimi distribution.

generality) on eigenvectors of Eq. (6) purely incoming from the left this implies

$$\begin{pmatrix} Q_{ll}(E) & Q_{rl}(E) \\ Q_{lr}(E) & Q_{rr}(E) \end{pmatrix} \begin{pmatrix} |\tau_i^{EWS}\rangle_l \\ 0 \end{pmatrix} = \tau_i^{EWS} \begin{pmatrix} |\tau_i^{EWS}\rangle_l \\ 0 \end{pmatrix} \tag{7}$$

and hence

$$Q_{ll}(E)|\tau_i^{EWS}\rangle_l = \tau_i^{EWS}|\tau_i^{EWS}\rangle_l, \tag{8a}$$

$$\big|Q_{lr}(E)|\tau_i^{EWS}\rangle_l\big| =: \chi_i \tau_i = 0, \tag{8b}$$

where we have defined the dimensionless null-space norm χ_i as a quantitative indicator of how well Eq. (8b) is numerically fulfilled for a given eigenstate i [8]. The constraint that $|\tau_i^{EWS}\rangle$ lies in the kernel of $Q_{lr}(E)$ [Eq. (8b)] also implies that those eigenvalues of the $N \times N$ transmission matrix $T = t^\dagger t$, t_i, $i = 1, \ldots, N$ corresponding to ray states are either close to $t_i = 0$ or $t_i = 1$ representing noiseless states [21]. Only a (typically small) subset of the eigenstates of Eq. (8a) will satisfy the additional condition of Eq. (8b). The latter provides a measure χ_i on how "particlelike" they are. Only quantum states with a small χ_i [Eq. (8b)] correspond to states that can be accommodated by the volume of phase space occupied by bundles of classical trajectories and pass through the scattering structure with collimated raylike wave fronts (see Fig. 2 below). Numerically we expect $\chi \ll 1$ for particlelike states. We find $\chi < 0.05$ for states with eigenvalues at the classical runtimes of the three bundles (A,B,C), while on average $\langle\chi\rangle \approx 0.2$. The remaining eigenstates of Eq. (8a) lack a clear association with specific classical path bundles but rather display seemingly random wave patterns [8].

The eigenvalues of Eq. (6), the eigentime delays (or dwell times) τ_i^{EWS} satisfy the sum rule [22]

$$\rho(E) = \frac{1}{\hbar} \sum_i \tau_i^{\text{EWS}} = \frac{1}{\hbar} \text{Tr } Q, \qquad (9)$$

with $\rho(E)$ the density of states of the scattering system. This sum rule obviously constraints possible fluctuations in the dwell time spectra.

III. THE TRUNCATED MODE BASIS EXPANSION

The challenge is now to calculate $S(E)$ [Eq. (4)] and $Q(E)$ [Eqs. (1) and (5)] for these large-scale structures containing millions of atomic sites. Since the flux through such a scattering structure is expected to be carried by transverse modes similar to those for ribbons of the given width D of infinite length, Bloch states are a well-suited basis for such calculations. However, for a given width D and energy E the number of Bloch states with arbitrary and, in general, complex k is as large as the number of tight-binding orbitals. Therefore, a truncation of this basis to a much smaller sized set of functions is required to render the calculation feasible. Key to this reduction is that the flux is carried predominantly by propagating rather than by evanescent modes. Accordingly, in the absence of short-range defects, Bloch states with (almost) real wave vectors with $|\exp(ikx)| \approx 1$ dominate the scattering problem. Guided by this criterion we truncate the Bloch basis, thereby substantially reducing computational cost. To obtain the desired reduced basis set, we solve the sparse eigenproblem of the infinite waveguide [23] iteratively for selected eigenvalues and eigenstates.

We consider a waveguide formed by a supercell containing N_c atomic sites infinitely repeated in x direction. The width of this supercell in y direction defines the width of the waveguide. Tight-binding couplings between two sites within one unit cell are described by an $N_c \times N_c$ matrix H_0, and coupling to neighboring unit cells by $N_c \times N_c$ matrices H_L and $H_R = H_L^\dagger$. We choose the cell size sufficiently large as to restrict couplings to neighboring supercells. For up to third-nearest-neighbor tight binding, a single armchair chain of carbon atoms can serve as the supercell. Starting from such a single armchair chain with, e.g., the length of 1 μm containing $N_c \approx 10\,000$ atoms a zigzag graphene ribbon of the same width can be built up by periodic repetition of the armchair chain in the direction perpendicular to the chain. The Hamiltonian of the entire waveguide can be schematically written as

$$H = \begin{pmatrix} \ddots & & & & \\ & H_0 & H_L & & \\ & H_R & H_0 & H_L & \\ & & H_R & H_0 & \\ & & & & \ddots \end{pmatrix}. \qquad (10)$$

The energy eigenvalue problem $H\Psi = E\Psi$ is solved with a Bloch ansatz,

$$\Psi = (\ldots, \psi_{-\Delta x}, \psi_0, \psi_{\Delta x}, \ldots)^T, \quad \psi_{\Delta x} = e^{ik\Delta x}\xi(k), \quad (11)$$

with $\chi(k) \in \mathbb{C}^{N_c}$ the vector of expansion coefficients in tight-binding orbitals defining the periodic part of the Bloch ansatz

on the unit cell. Assuming H_L to be invertible, Eqs. (10) and (11) result in a linear eigenvalue problem [23] of size $2N_c \times 2N_c$, i.e., of size $20\,000 \times 20\,000$ for a 1 μm wide ribbon,

$$\begin{pmatrix} -H_L^{-1}(H_0 - E) & -H_L^{-1}H_R \\ \mathbb{1} & 0 \end{pmatrix} \begin{pmatrix} \eta \\ \xi \end{pmatrix} = \lambda \begin{pmatrix} \eta \\ \xi \end{pmatrix}. \qquad (12)$$

The block structure of Eq. (12) results from rewriting a quadratic eigenvalue problem as a linear problem of double the size with $\eta = \lambda\xi$. It should be noted that the block structure Eq. (12) is entirely unrelated to the block structure of Eq. (8). The block structure in Eq. (12) is identical to the one appearing in approaches for parabolic dispersion [24], with the general tight-binding matrices H_0 and $H_{L,R}$ replacing the simpler tridiagonal matrices. If H_L is noninvertible, one has to solve a generalized eigenproblem or has to eliminate the surplus dimensions using a singular value decomposition [25]. Equation (12) is typically solved for all $2N_c$ eigenvalues and corresponding eigenvectors, which allows for a straightforward representation of the scattering problem [23,24,26].

We are interested here in the case where the number of orbitals (or sites) is so large as to render such an approach unfeasible. For the present problem only those states with eigenvalues featuring a magnitude close to unity are physically relevant for transport. We can therefore reduce the numerical problem by focusing on finding all eigenvalues of Eq. (12) close to the unit circle. Arnoldi iterations using multiple shifts have been suggested as a possible approach [27]. However, depending on the distribution of the propagating eigenvalues on the unit circle, one might need a prohibitively large number of shifts to find all N_{open} open modes. Instead, we employ a Davidson iteration [28] to locate the eigenvalues close to $|\lambda| = 1$. The algorithm involves the iterative and approximate solution of

$$(A - \lambda_i \mathbb{1})(\mathbf{v}_i - \mathbf{r}_i) = 0$$

for the residue $\mathbf{r}_i$ which constitute the "missing" complement for a set of m guesses for the eigenvectors $\mathbf{v}_i$ of A. The approximate eigenvalues λ_i are obtained by projecting A onto the basis of size $2m$ spanned by the $\mathbf{v}_i$ and $\mathbf{r}_i$. In each iteration step we keep m (here we choose $m = 8$) eigenvalues λ_i closest to the unit circle, with smallest $|\text{Re}[\log(\lambda_i)]|$. The search space of the $\mathbf{v}_i$ and $\mathbf{r}_i$ is always kept orthogonal to eigenvectors already converged. To accelerate the convergence we switch to an inverse iteration whenever the Jacobi-Davidson residuals are low and the eigenvalues have been successfully located. Factorizing a sparse matrix is still easily possible for the system sizes considered here. With this eigensolver we can efficiently identify propagating (and weakly evanescent) modes of any tight-binding Hamiltonian of (almost) any size. More generally, this approach successfully locates eigenvalues of a matrix in nontrivial regions of the spectrum. We run the algorithm until we have assembled our truncated mode basis (TMB) using a number N_{TMB} of Bloch states with the smallest imaginary $|\text{Im}k|$, i.e., the open and most weakly evanescent modes. In the present case we use $N_{\text{TMB}} = 2N_{\text{open}} \ll N_c$ since weakly evanescent modes can significantly contribute to transport in graphene [29–32].

Since the Green's function of the ribbon should be dominated by the open modes, the truncated set of Bloch states we

have determined could directly be used to solve the scattering problem. However, such an approach, while possible, yields a truncated scattering problem that is no longer unitary. While it would seem that the impact of the neglected modes is small (and could be made negligible by further increasing N_{TBM}), we find that, in particular, energetically close to resonances, the resulting transmission features unphysically large values. The underlying reason is the difficulty to enforce the orthogonality condition for the Bloch eigenstates η_i. Since the eigenproblem of Eq. (12) is non-Hermitian, one has to distinguish between left-sided and right-sided eigenvectors. If only a subset of right-sided eigenvectors is calculated, the corresponding orthogonal complement $\bar{\eta}$ with $\bar{\eta}_i \cdot \bar{\eta}_j = \delta_{ij}$ cannot be unambiguously determined. This is particularly problematic when evaluating the energy derivative of the scattering matrix to determine the Wigner-Smith operator. To eschew this problem entirely, and to obtain an exactly unitary scattering matrix, we project the original scattering problem expressed in terms of the tight-binding orbital basis of the Hamiltonian Eq. (2) onto the orthogonalized and truncated mode basis $\{v_i\}$ for each supercell,

$$(\mathcal{H}_0)_{ij} = \langle v_i | H_0 | v_j \rangle, \quad i = 1, \ldots, N_{\text{TMB}} \quad (13)$$

and, correspondingly, for H_L and H_R. The resulting matrices $\mathcal{H}$ define a new scattering problem of much smaller dimensions that can now be solved exactly, providing a unitary solution. A similar mode basis approach has been previously suggested [33], though without truncation. We solve the scattering problem within the reduced basis via the standard recursive Green's function algorithm [19,25]. With the present approach we are able to calculate the S and Q matrices introduced above for large structures from atomic-scale input [Eq. (2)] provided they can be assembled from rectangular building blocks (Fig. 1).

IV. RESULTS OR THE TIME-DELAY SPECTRUM OF RAY-SCATTERING STATES

Short trajectories with correspondingly short dwell times in the quantum dot (Fig. 1) are expected to feature ray scattering states most prominently as their associated bundles can occupy a large volume in phase space [9]. We therefore search for the eigenstates of $Q_{ll}(E)$ with small eigenvalues τ^{EWS}. We label the eigenvalues $\tau_{t/r,b}^{\text{EWS}}$ by their exit channel (r reflected, t transmitted) and by the number of bounces b at the internal walls. The dwell time of the classical path A (Fig. 1) corresponds to the eigenvalue $\tau_{t,0}^{\text{EWS}}$, of path B to $\tau_{r,1}^{\text{EWS}}$ and of path C to $\tau_{t,2}^{\text{EWS}}$.

An additional "quantum" number will now be added as we find the smallest eigenvalue $\tau_{t,0}^{\text{EWS}}$ to be (nearly) doubly degenerate. The corresponding pair of eigenstates (Fig. 2) closely retraces the ray for direct transmission through the structure [Fig. 1(a)]. To unravel the origin of this eigentime degeneracy, we analyze the physics of these ray-scattering states in phase space in terms of their Husimi distributions [18]. The Husimi distribution of a wave function in site (or
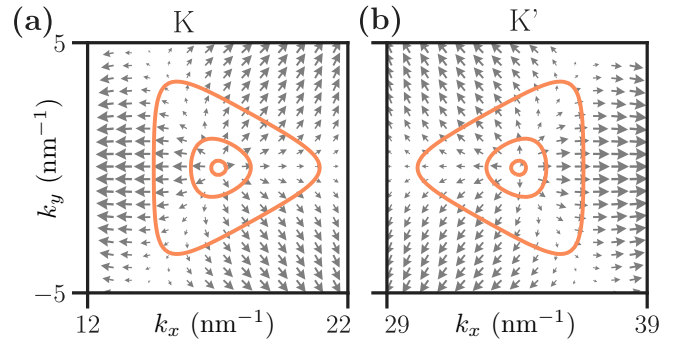

FIG. 3. Vector field of group velocities (gray arrows) near the K valley (a) and the K' valley (b). In orange are the energy contours at the energies $E_1 = 0.15$ eV, $E_2 = 0.59$ eV, and $E_3 = 1.49$ eV which we consider in our simulations.

coordinate) representation $\{\psi_j\}$ is given by

$$\mathfrak{H}[\psi](r_0, k_0; \sigma) = \frac{1}{\pi} \left| \sum_j \psi_j \exp^{\left(\frac{r_j - r_0}{4\sigma^2}\right)} \exp^{ik_0 r_0} \right|^2, \quad (14)$$

where the sum runs over the site index j and ψ_j is the wave-function amplitude at tight-binding site j. The Husimi distribution $\mathfrak{H}[\psi]$ provides a visualization of the quantum-mechanical scattering states in terms of a positive semi-definite probability density at the coordinates (r_0, k_0) in the classical phase space. σ defines the width of the minimum-uncertainty wave packet the underlying Wigner distribution [34] is averaged over. For quantum billiards, $\mathfrak{H}[\psi]$ is a four-dimensional distribution. By fixing the x coordinate to the center of the structure, $x = L/2$, and integrating $\mathfrak{H}[\psi]$ over all y, we obtain a reduced Husimi distribution in k space that characterizes the interior of the scattering structure which is least affected by diffractive scattering at the lead openings. We find the projected Husimi distribution to be well localized on the energy contours of the bulk band structure of graphene corresponding to the scattering energy E [Figs. 2(b) and 2(d)]. More remarkably, this distinct point of localization of the Husimi distribution of the particlelike state on the contour is determined by the requirement that the orientation of the group velocity vector $v_g = \partial_k E(k)$ (Fig. 3) matches the propagation direction of the classical particle. By contrast, the Husimi distribution of states which do not propagate along classical trajectories or of states which do not fulfill Eq. (8b), is spread out over large portions of the energy contour. Furthermore, the Husimi representation helps us to clearly identify the origin of the pair of the (near) degenerate ray scattering states of Fig. 2: the two time-delay eigenstates reside on different Dirac cones near K and K'. These quasiclassical particlelike or raylike states unambiguously carry also the information on the valley quantum degree of freedom. Thus, the eigenstates of the time-delay operator feature also well-defined valley quantum numbers $|\tau_{t,0,\sigma}^{\text{EWS}}\rangle$, with $\sigma = K, K'$. The eigentime splitting between the two states implies that the particle can be transported either in the "faster" valley with a larger group velocity and slightly lower dwell time or in the "slower" valley with smaller group velocity and, correspondingly, larger dwell time.
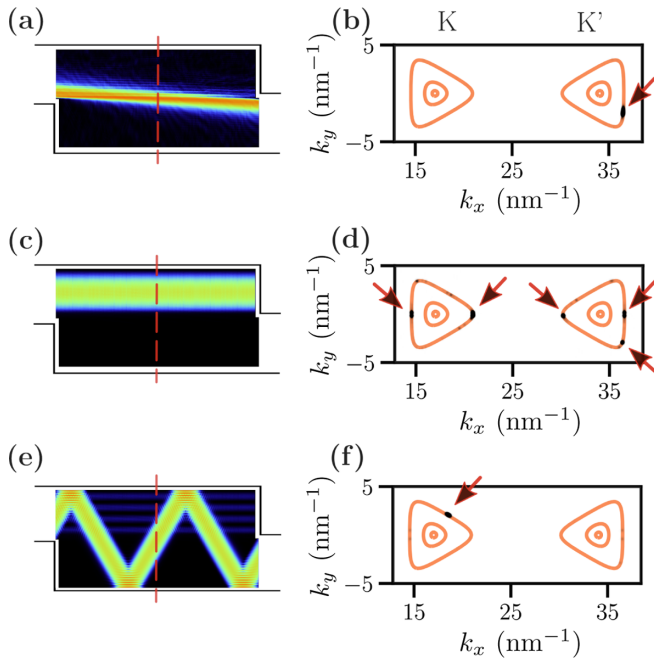
FIG. 4. Left panels: real space wave function amplitudes of selected Eisenbud-Wigner-Smith time-delay operator eigenfunctions for the 60 nm wide ribbon. The quantum states (a), (c), and (e) propagate along the classical trajectories (A), (B), (C) of Fig. 1(f). The Husimi distributions (right panels) are evaluated at $x = L/2$, averaged over y, as indicated by the red dashed line in (a), (c), and (e). The Husimi distribution corresponding to the wave functions are plotted in black and the energy contour lines of the bulk band structure in orange. For raylike states, the Husimi distribution is strongly localized with the black spot representing 90% of the weight of $\mathfrak{H}[\psi](\mathbf{k}_0)$. In the reflecting state (c) and (d), a small admixture of a transmitting state (b) is visible in the Husimi distribution [bottom right arrow in (d)].

At a relatively high scattering energy of $E = 1.5$ eV above the Dirac point well into the regime of pronounced trigonal warping of the band structure, the sensitivity of the ray-scattering states to the valley degree of freedom becomes enhanced (Fig. 4): the directly transmitting ray (A) [Fig. 4(a)] resides now exclusively in the K' valley, i.e., $|\tau_{t,0,K'}^{\text{EWS}}\rangle$ since on the corresponding energy contour of the K valley not enough k space volume with the group velocity vector needed for the direct ray can be found. Conversely, a significant k space volume for propagation at an angle of $60°$ is available, which results in a stable ray which is 4 times specularly reflected (trajectory C) at the zigzag boundary as fastest state on the K cone, i.e., $|\tau_{t,4,K}^{\text{EWS}}\rangle$ [Fig. 4(c)]. The preference for $60°$ injection is an immediate consequence of the trigonal warping which results in a strongly anisotropic group velocity distribution (see Fig. 3). Even for longer ribbons, the fastest ray state in the K valley always propagates at a $60°$ angle, making as many bounces as required to reach the exit lead. By contrast, the directly reflected ray (B) must undergo backscattering at the armchair boundary. Unlike the zigzag boundary, the armchair boundary couples the K and K' valleys. Consequently, the one-bounce reflected ray is a coherent superposition of the ray states $|\tau_{r,1,K}^{\text{EWS}}\rangle$ and $|\tau_{r,1,K'}^{\text{EWS}}\rangle$ living in different valleys.

Imperfections at the boundaries will likewise result in a mixture of valley states for ray states that scatter at the boundary, with superpositions determined by the precise reflection properties of the boundaries as well as the difference in group velocities between the two valleys. Also scattering states that do not fulfill the requirement of noiseless states [Eq. (8b)] are, in general, not valley polarized. Avoiding a mixing of valley states could be possible for sufficiently smooth boundaries that lack the high Fourier components required to scatter between valleys, as created, e.g., by electrostatic confinement in the case of bilayer graphene [35].

To systematically study the variation of the particlelike scattering states as a function of the energy of the scattered particle E and the length L of the cavity, we focus now on the statistical distribution of eigenvalues of the time-delay operator $Q_{ll}(E)$ (Fig. 5). To remove the purely geometric dependence on the path length we rescale all eigenvalues by $\tau_0 = L/v_0$ as in the classical case [see Fig. 1(f)] where now v_0 is the largest group velocity of all N open channel modes, $v_0 = \max(v_g)$. For a comparison with the transport through a quantum dot that features (near the Γ point) a quadratic rather than a linear dispersion [see Figs. 1(c) and 1(d)] we also calculate [Fig. 5(d)] the time-delay eigenvalue distribution for a ribbon built from a material with a square rather than hexagonal lattice. In Fig. 5 we have color coded the eigentime distribution in the $(\tau/\tau_0, L/D)$ plane by their raylike character. Raylike states with small null-space norm χ [Eq. (8b)] appear purple (dark), nonclassical scattering states with large null-space norm appear yellow (light). Obviously ray states evolve continuously as a function of L/D approaching an integer value of τ/τ_0 with increasing L/D. This dependence closely mimics the variation of the dwell time of classical trajectories with L/D [Fig. 1(f)]. By contrast, the states with large χ appear broadly and quasirandomly distributed forming a "background." They correspond to time-delay eigenstates that cannot be unambiguously assigned a single classical path bundle of phase space volume sufficient to accommodate at least one quantum state.

To further elucidate the relationship between classical bundles and raylike states, we focus now on the subset of ray states (null-space norm $\chi < 0.25$). We separate the eigentime distribution according to their raylike (r, t) and valley (K, K') quantum numbers through color and symbol coding (Fig. 6). The bounce number b can be inferred from the values of scaled eigentimes. For the square lattice, eigenvalues are only color coded by r/t as the valley degree of freedom is absent. The one-bounce classical reflection path (B) (Fig. 1) at $\tau/\tau_0 = 2$ is present in the time-delay spectra for all $L/D \geqslant 0$. The direct transmission path (A) near $\tau/\tau_0 = 1$ as well as the two-bounce path near $\tau/\tau_0 = 3$ appear for obvious geometric reasons (Fig. 1) only for $L/D > 0$. The histograms of the time-delay distribution generated by projecting all eigenvalues onto the τ/τ_0 axis also shown in Fig. 6 feature clearly visible peaks corresponding to prominent few-bounce bundles. The most important difference between graphene ribbons of different width D [Figs. 6(a)–6(c)] and the square-lattice ribbon [Fig. 6(d)] is the splitting of these peaks by the valley degree of freedom. States propagating in one valley are consistently slower than states in the other valley. Their different dwell times are due to different group velocities $1/\hbar \cdot \partial_{\mathbf{k}} E$, resulting
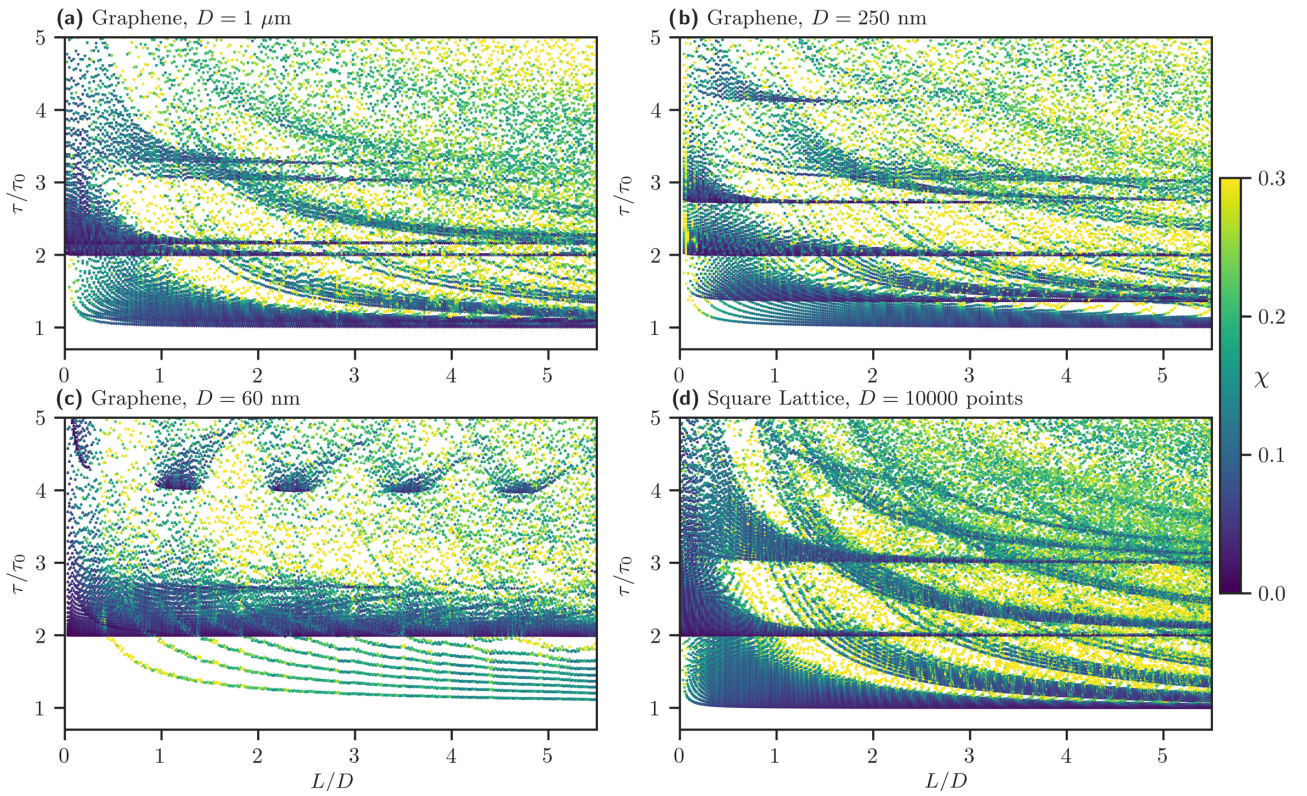
FIG. 5. Scaled Eisenbud-Wigner-Smith time-delay eigenvalues τ/τ_0 as a function of cavity length. For a comparison the time-delay spectrum for a ribbon with that of a square lattice is shown in (d). (a) $E = 0.15$ eV with $D = 1\,\mu$m, (b) $E = 0.59$ eV with $D = 250$ nm, and (c) $E = 1.5$ eV with $D = 60$ nm. Color scale corresponds to the null-space norm χ, Eq. (8b), see color bar.

from trigonal warping. It is worth noting that the variation of the splitting with D [Figs. 6(a)–6(c)] is not a geometric effect but a band structure effect resulting from probing different regions of trigonal warping as E varies with D for a fixed number of open channels.

The valley splitting of the eigentimes is already a 5 % effect even at relatively low energies of $E = 150$ meV. At higher energies $E = 0.59$ eV [$D = 250$ nm, Fig. 6(b)] states in one valley are about 1.4 times slower than in the other valley. More modes appear in the faster valley indicating that more phase space volume is available. For even larger energies of $E = 1.5$ eV [Fig. 6(c)] the peak associated with the "slower" valley has almost completely disappeared because of the mismatch with the group velocity vector required for the direct transmission path (see Fig. 4). Instead, time-delay eigenstates near $\tau/\tau_0 = 2$ and near $\tau/\tau_0 = 4$ are associated with multibounce bundles contributing to transmission and reflection, respectively. These rays appear periodically as a function of L/D whenever trajectories multiply specularly reflected with $60°$ at the zigzag boundary can reach the exit lead. The propensity for $60°$ scattering is a direct result of band structure anisotropy as trigonal warping results in three highly stable propagation directions per valley.

While a subset of eigenvalues τ^{EWS}, in particular in the lower part of the time spectrum, evolve continuously as a function of L/D in accord with the dwell time of classical paths, the behavior of most other, in particular larger, eigentimes appears to be random. Those states do not propagate

along classical paths and fail to fulfill Eq. (8b). The seemingly random time-delay distribution plays, however, a crucial role for the set of all eigenvalues to satisfy the eigentime sum rule of Eq. (9). In fact, we find that they obey a stronger sum rule for the time-delay matrix restricted to incoming scattering states from the left lead only,

$$\rho(E) \approx \frac{1}{\hbar}\mathrm{tr}Q(E) \approx \frac{2}{\hbar}\mathrm{tr}Q_{ll}(E) = \frac{1}{\hbar}\sum_{i=1}^{N}\tau_i^{\mathrm{EWS}}(E). \quad (15)$$

Remarkably, this holds for both the square lattice and for graphene even though the corresponding densities of states and typical dwell times fundamentally differ. For a square lattice with quadratic dispersion near the Γ point, $\rho^{\mathrm{square}}(E)$ scales in 2D as

$$\rho^{\mathrm{square}}(E) = \frac{m^*}{\pi\hbar^2}, \quad (16a)$$

i.e., is independent of E, while for graphene near the Dirac point

$$\rho^{\mathrm{graphene}}(E) = \frac{2}{\pi v_{\mathrm{F}}^2}|E|. \quad (16b)$$

The classical dwell time $\tau_{\mathrm{cl}} = s/v$ (with s the path length) scales for quadratic dispersion with energy as

$$\tau_{\mathrm{cl}}^{\mathrm{square}} \propto v^{-1} \propto E^{-\frac{1}{2}}, \quad (17a)$$
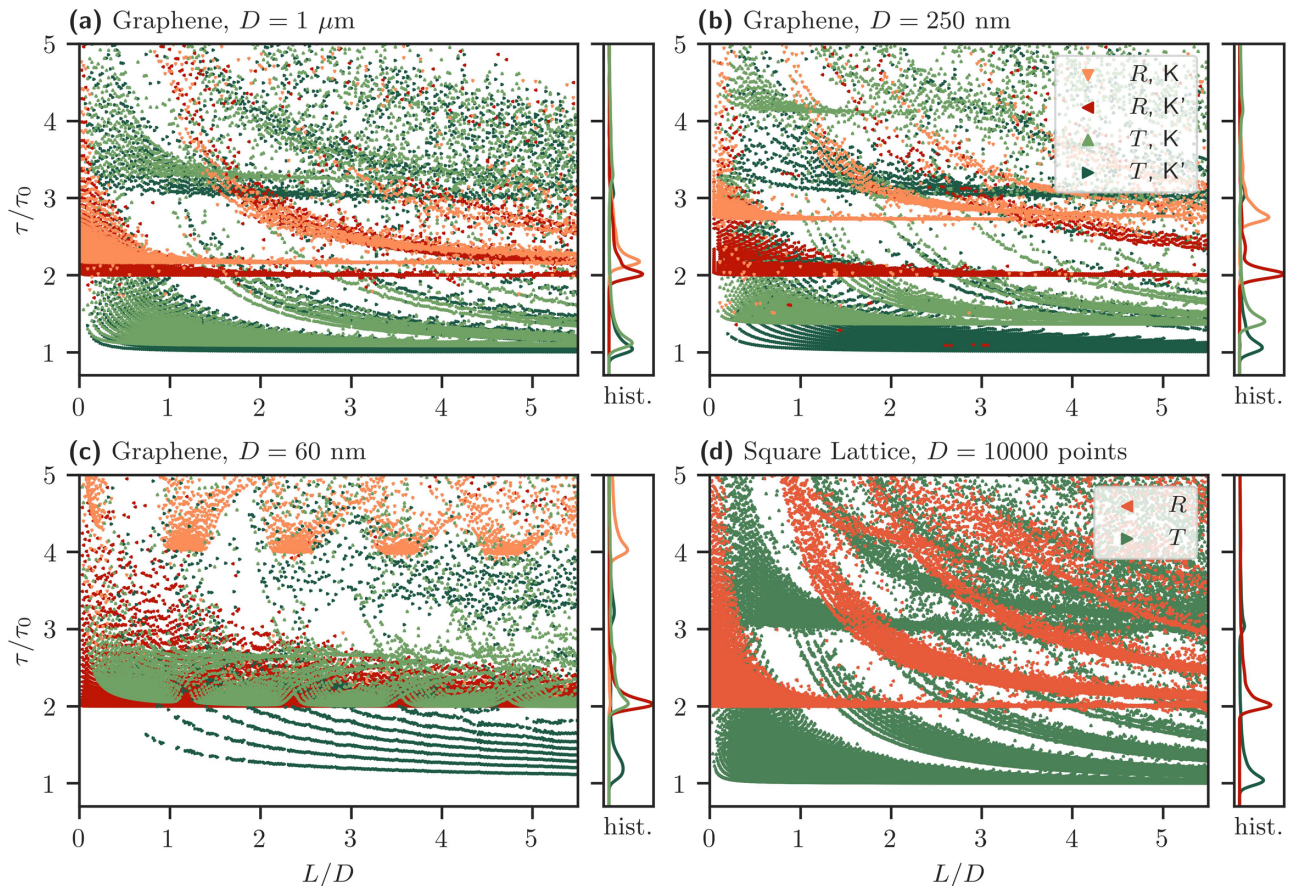
FIG. 6. Scaled Eisenbud-Wigner-Smith time-delay eigenvalues τ/τ_0 as a function of cavity length for the data sets of Fig. 5, however, restricted to raylike states with eigenvalues $\chi \leqslant 0.25$. Symbol color encodes transmission, reflection, and valley character (graphene only): transmitted [light (K) and dark (K') green] and reflected [red (K) or orange (K')] states. Valley character is evaluated for the incoming wave, and assigned to the dominant contribution. Right subpanels: histograms of the distribution of the time delays projected onto the τ/τ_0 axis. The time-delay eigenvalues associated with bundles result in a peak at the asymptotic ($L \to \infty$) classical dwell times. Differences in dwell times results in a peak splitting due to the valley degree of freedom [see (a) and (b)]. In (c), the $60°$ transmission path has the same transmission time as the one-bounce reflection path, as expected classically.

while for ultrarelativistic Dirac particles with velocities independent of energy,

$$\tau_{\mathrm{cl}}^{\mathrm{graphene}} = \mathrm{const.}, \qquad (17b)$$

i.e., $\tau_{\mathrm{cl}}^{\mathrm{graphene}}$ is independent of energy. As the eigentime values of the raylike states as well as the average over all eigenvalues $\langle \tau^{\mathrm{EWS}} \rangle$ closely follow the classical predictions [Eq. (17)], it is, at first glance, surprising that in view of Eqs. (16) and (17) the sum rule [Eq. (15)] holds. Key to the resolution of this apparent contradiction is the observation that the sum over all τ^{EWS} and the average $\langle \tau^{\mathrm{EWS}} \rangle$ feature a different energy dependence (Fig. 7). While the energy dependence of the average $\langle \tau^{\mathrm{EWS}} \rangle$ [Figs. 7(a) and 7(b)] closely mirror the energy dependence of the eigendwelltime of the raylike scattering states [Figs. 7(c) and 7(d)], the sum [Figs. 7(a) and 7(b)] displays a different energy dependence, which is consistent with $\rho(E)$. This difference originates from the number of open channels N and, thus, the number of terms in the sum [Eq. (15)]. Since $N \propto k$ [see Eq. (3)], for quadratic dispersion N scales as $N^{\mathrm{square}} \propto \sqrt{E}$ while for the Dirac cone $N^{\mathrm{graphene}} \propto |E|$. It is therefore the variation of the number of eigenvalues

as a function of energy, in particular the presence of those with "randomly" distributed large dwell times, that enforces the validity of the sum rule.

V. SUMMARY AND OUTLOOK

We have investigated an unconventional class of scattering states through open graphene quantum dots that closely mimics beams of geometric electron ray optics. They emerge as eigenstates of the Eisenbud-Wigner-Smith time-delay operator in the subspace of incoming scattering states from the source lead and are (approximately) noiseless. These raylike states can be uniquely characterized by the exit channel they approach (either transmission or reflection), by the number of specular reflections at the internal walls of the cavity, and, specific to graphene, by the quantum number associated with the valley degree of freedom. Ray scattering states can be constructed that propagate exclusively in one valley or a coherent superposition of both valleys. This observation raises the perspective of realizing particlelike valleytronics. Generating raylike scattering states requires a large number of open modes and, correspondingly, relatively high excitation
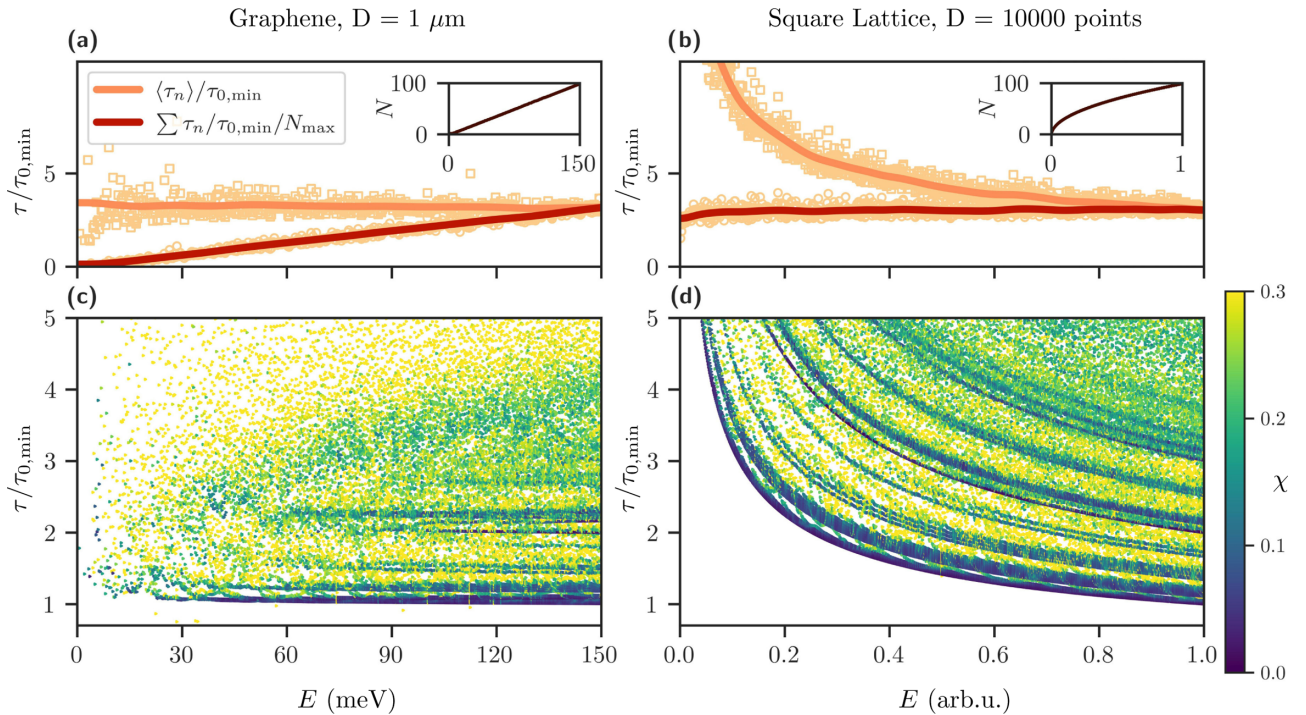
FIG. 7. Time-delay eigenvalues as function of energy E for a ribbon of length $L/D = 3$. (a) and (c): graphene lattice with $D = 1\ \mu$m; (b) and (d) square lattice with $D = 1000$ points. (a) and (b): average scaled dwell time $\langle \tau^{\mathrm{EWS}} \rangle$ (orange) in units of the lowest possible transit time $\tau_{t,0,v} = L/v_{g,\max}$ where $v_{g,\max}$ is the highest group velocity in the square lattice at the highest injection energy E and the sum over all scaled dwell times (red) normalized to the number of open channels $N = 99$ at the largest energy [$E = 150$ meV in (b)]. Insets show the number of open modes N as a function of energy E. The color of the time-delay eigenvalues in (c) and (d) is chosen as in Fig. 5, displaying the null-space norm χ, Eq. (8b).

energies. Forming suitable coherent superpositions of such degenerate states in the entrance channel appear currently to be the major challenge on the way to their realization. Optical excitation by shaped pulses in biased structures might be a promising avenue.

Trigonal warping of the Dirac cones in the band structure of graphene is found to play an important role in the valley selectivity but also in the directional preference and the speed with which particlelike transport through the graphene ribbon proceeds. Comparison with transport through a ribbon assembled from a square lattice featuring a quadratic dispersion shows that the typical eigentime delays τ^{EWS} feature a very similar scaling with the length of the ribbon but a strongly different scaling with energy. For both systems we find the sum rule for eigentime delays to be satisfied for the time-delay operator restricted to the subspace of incoming scattering from one lead. The present method allowing simulation of micrometer-sized devices starting from a atomic-orbital based tight-binding Hamiltonian is currently applicable for structures built-up from rectangular building blocks. It can be applied also to other ribbons featuring a hexagonal lattice and trigonal distortion of the band structure, in particular bilayer graphene, where a similar nonisotropic dynamics as the one investigated here is expected to unfold. Future extensions to other geometries can be envisioned as well.

Experimentally preparing "pure" eigenstates of the time-delay operator appears currently an experimental challenge. Nevertheless, this newly identified class of states is expected

to play a key role in the analysis of charge transport, for example in optically excited graphene structures [36]. The electronic excitation by an ultrashort optical pulse will create wave packets that can be conveniently expanded in terms of a superposition of such time-delay eigenstates rather than standard scattering states. Varying the location of pump and probe, the current response observed at short pump-probe delays is expected to be determined by the ray states with the shortest dwell time. Along similar lines, graphene has been suggested as material for high-frequency nanoelectronics (see, e.g., Ref. [37]) with graphene nanotransistors operating at frequencies of $\approx$155 GHz. The corresponding oscillation periods are of the same order of magnitude as the time-delay differences between the two valley states we are reporting here.

It should be emphasized that the appearance and key properties of the ray states with short Eisenbud-Wigner-Smith time-delay eigenvalues do not critically depend on the realization of perfect zigzag and armchair edges of the ribbon assumed here for reasons of computational simplicity and clarity. Graphene structures with atomically cleanly defined edges can be synthesized by bottom-up approaches [38], however fabrication of large-scale devices with precise edges remains challenging. In fact, the direct ray with the shortest time delay occupying the largest volume in phase space (ray A in Fig. 1, see also Fig. 2) does not touch the (im)perfect internal boundaries of the cavity at all. More generally, a limited number of diffractive scatterings at isolated point defects will distort but not completely destroy the classical bundles that

accommodate the quantum ray states. Furthermore, bilayer graphene devices can be realized with electrostatic definition of scattering geometries featuring smooth edges [35]. As the key features of the ray states in graphene are determined by the triangular distortion of the band structure in k space but not by the geometry of the edges in real space, a similar non-isotropic dynamics as observed here should unfold in bilayer graphene where a pronounced triangular distortion appears at very low energies [39].

ACKNOWLEDGEMENTS

[1] R. Landauer, Spatial variation of currents and fields due to localized scatterers in metallic conduction, IBM J. Res. Dev. **1**, 223 (1957).

[2] M. Büttiker, Absence of backscattering in the quantum Hall effect in multiprobe conductors, Phys. Rev. B **38**, 9375 (1988).

[3] S. W. McDonald and A. N. Kaufman, Spectrum and Eigenfunctions for a Hamiltonian with Stochastic Trajectories, Phys. Rev. Lett. **42**, 1189 (1979).

[4] C. M. Marcus, A. J. Rimberg, R. M. Westervelt, P. F. Hopkins, and A. C. Gossard, Conductance Fluctuations and Chaotic Scattering in Ballistic Microstructures, Phys. Rev. Lett. **69**, 506 (1992).

[5] H. U. Baranger, R. A. Jalabert, and A. Douglas Stone, Quantum-chaotic scattering effects in semiconductor microstructures, Chaos: Interdisc. J. Nonlinear Sci. **3**, 665 (1993).

[6] H. Ishio and J. Burgdörfer, Quantum conductance fluctuations and classical short-path dynamics, Phys. Rev. B **51**, 2013 (1995).

[7] M. Schmitz, S. Engels, L. Banszerus, K. Watanabe, T. Taniguchi, C. Stampfer, and B. Beschoten, High mobility dry-transferred CVD bilayer graphene, Appl. Phys. Lett. **110**, 263110 (2017).

[8] S. Rotter, P. Ambichl, and F. Libisch, Generating Particlelike Scattering States in Wave Transport, Phys. Rev. Lett. **106**, 120602 (2011).

[9] L. Wirtz, J.-Z. Tang, and J. Burgdörfer, Geometry-dependent scattering through ballistic microstructures: Semiclassical theory beyond the stationary-phase approximation, Phys. Rev. B **56**, 7589 (1997).

[10] E. J. Heller, Bound-State Eigenfunctions of Classically Chaotic Hamiltonian Systems: Scars of Periodic Orbits, Phys. Rev. Lett. **53**, 1515 (1984).

[11] M. C. Gutzwiller, *Chaos in Classical and Quantum Mechanics, Interdisciplinary Applied Mathematics* (Springer, Berlin, 1990).

[12] L. Huang, Y.-C. Lai, D. K. Ferry, S. M. Goodnick, and R. Akis, Relativistic Quantum Scars, Phys. Rev. Lett. **103**, 054101 (2009).

[13] X. Ni, L. Huang, Y.-C. Lai, and C. Grebogi, Scarring of Dirac fermions in chaotic billiards, Phys. Rev. E **86**, 016702 (2012).

[14] A. H. Castro Neto, F. Guinea, N. M. R. Peres, K. S. Novoselov, and A. K. Geim, The electronic properties of graphene, Rev. Mod. Phys. **81**, 109 (2009).

[15] E. P. Wigner, Lower limit for the energy derivative of the scattering phase shift, Phys. Rev. **98**, 145 (1955).

[16] L. Eisenbud, The Formal Properties of Nuclear Collisions, PhD. thesis, Princeton University, 1948.

[17] F. T. Smith, Lifetime matrix in collision theory, Phys. Rev. **118**, 349 (1960).

[18] K. Husimi, Some formal properties of the density matrix, Proc. Phys.-Math. Soc. Jpn. 3rd Ser. **22**, 264 (1940).

[19] F. Libisch, S. Rotter, and J. Burgdörfer, Coherent transport through graphene nanoribbons in the presence of edge disorder, New J. Phys. **14**, 123006 (2012).

[20] L. Linhart, J. Burgdörfer, and F. Libisch, Accurate modeling of defects in graphene transport calculations, Phys. Rev. B **97**, 035430 (2018).

[21] S. Rotter, F. Aigner, and J. Burgdörfer, Statistics of transmission eigenvalues in two-dimensional quantum cavities: Ballistic versus stochastic scattering, Phys. Rev. B **75**, 125312 (2007).

[22] G. Iannaccone, General relation between density of states and dwell times in mesoscopic systems, Phys. Rev. B **51**, 4727 (1995).

[23] S. Sanvito, C. Lambert, J. H. Jefferson, and A. Bratkovsky, General Green's-function formalism for transport calculations with spd Hamiltonians and giant magnetoresistance in Co- and Ni-based magnetic multilayers, Phys. Rev. B **59**, 11936 (1999).

[24] T. Ando, Quantum point contacts in magnetic fields, Phys. Rev. B **44**, 8017 (1991).

[25] I. Rungger and S. Sanvito, Algorithm for the construction of self-energies for electronic transport calculations based on singularity elimination and singular value decomposition, Phys. Rev. B **78**, 035407 (2008).

[26] H.-Y. Deng and K. Wakabayashi, Decomposition into propagating and evanescent modes of graphene ribbons, Phys. Rev. B **90**, 045402 (2014).

[27] H. H. B. Sørensen, P. C. Hansen, D. E. Petersen, S. Skelboe, and K. Stokbro, Krylov subspace method for evaluating the self-energy matrices in electron transport calculations, Phys. Rev. B **77**, 155301 (2008).

[28] K. Hirao and H. Nakatsuji, A generalization of the Davidson's method to large nonsymmetric eigenvalue problems, J. Comput. Phys. **45**, 246 (1982).

[29] A. D. Wiener and M. Kindermann, Signatures of evanescent mode transport in graphene, Phys. Rev. B **84**, 245420 (2011).

[30] R. Danneau, F. Wu, M. F. Craciun, S. Russo, M. Y. Tomi, J. Salmilehto, A. F. Morpurgo, and P. J. Hakonen, Evanescent wave transport and shot noise in graphene: Ballistic regime and effect of disorder, J. Low Temp. Phys. **153**, 374 (2008).

[31] M. I. Katsnelson, Quantum transport via evanescent waves in undoped graphene, J. Comput. Theor. Nanosci. **8**, 912 (2011).

[32] M. I. Katsnelson, *The Physics of Graphene* (Cambridge University Press, Cambridge, 2020).

[33] R. Grassi, A. Gnudi, E. Gnani, S. Reggiani, and G. Baccarani, Mode space approach for tight binding transport simulation in graphene nanoribbon fets, IEEE Trans. Nanotechnol. **10**, 371 (2011).

[34] M. Hillery, R. F. O'Connell, M. O. Scully, and E. P. Wigner, Distribution functions in physics: Fundamentals, Phys. Rep. **106**, 121 (1984).

[35] H. Overweg, A. Knothe, T. Fabian, L. Linhart, P. Rickhaus, L. Wernli, K. Watanabe, T. Taniguchi, D. Sánchez, J. Burgdörfer, F. Libisch, V. I. Fal'ko, K. Ensslin, and T. Ihn, Topologically Nontrivial Valley States in Bilayer Graphene Quantum Point Contacts, Phys. Rev. Lett. **121**, 257702 (2018).

[36] T. Higuchi, C. Heide, K. Ullmann, H. B. Weber, and P. Hommelhoff, Light-field-driven currents in graphene, Nature (London) **550**, 224 (2017).

[37] Y. Wu, Y.-m. Lin, A. A. Bol, K. A. Jenkins, F. Xia, D. B. Farmer, Y. Zhu, and P. Avouris, High-frequency, scaled graphene transistors on diamond-like carbon, Nature (London) **472**, 74 (2011).

[38] J. Cai, P. Ruffieux, R. Jaafar, M. Bieri, T. Braun, S. Blankenburg, M. Muoth, A. P. Seitsonen, M. Saleh, X. Feng, K. Müllen, and R. Fasel, Atomically precise bottom-up fabrication of graphene nanoribbons, Nature (London) **466**, 470 (2010).

[39] A. Knothe and V. Fal'ko, Influence of minivalleys and Berry curvature on electrostatically induced quantum wires in gapped bilayer graphene, Phys. Rev. B **98**, 155435 (2018).